INTERNATIONAL JOURNAL FOR NUMERICAL METHODS IN FLUIDS
Int. J. Numer. Meth. Fluids 2010; **62**:854–874
Published online 25 March 2009 in Wiley InterScience (www.interscience.wiley.com). DOI: 10.1002/fld.2042

Direct numerical simulation of low Reynolds number flows in an open-channel with sidewalls

Younghoon Joung[1] and Sung-Uk Choi[2,*,†,‡]

[1]*ISAN Research Institute, ISAN Corporation, Gyeonggi-Do 431-060, Korea*
[2]*School of Civil and Environmental Engineering, Yonsei University, Seoul 120-749, Korea*

SUMMARY

A direct numerical simulation of low Reynolds number turbulent flows in an open-channel with sidewalls is presented. Mean flow and turbulence structures are described and compared with both simulated and measured data available from the literature. The simulation results show that secondary flows are generated near the walls and free surface. In particular, at the upper corner of the channel, a small vortex called inner secondary flows is simulated. The results show that the inner secondary flows, counter-rotating to outer secondary flows away from the sidewall, increase the shear velocity near the free surface. The secondary flows observed in turbulent open-channel flows are related to the production of Reynolds shear stress. A quadrant analysis shows that sweeps and ejections are dominant in the regions where secondary flows rush in toward the wall and eject from the wall, respectively. A conditional quadrant analysis also reveals that the production of Reynolds shear stress and the secondary flow patterns are determined by the directional tendency of the dominant coherent structures. Copyright © 2009 John Wiley & Sons, Ltd.

Received 16 June 2008; Revised 25 November 2008; Accepted 6 February 2009

KEY WORDS: direct numerical simulation; open-channel flows; sidewall; secondary flows; quadrant analysis; coherent structures

INTRODUCTION

Turbulent open-channel flows without sidewalls have only one inhomogeneous direction due to the free surface and the bottom. However, the presence of the sidewall increases the number of

*Correspondence to: Sung-Uk Choi, School of Civil and Environmental Engineering, Yonsei University, Seoul 120-749, Korea.
†E-mail: schoi@yonsei.ac.kr
‡Professor.

Contract/grant sponsor: Ministry of Science and Technology, Korea; contract/grant number: code No. 2-3-2

inhomogeneous directions, which further complicates the flow structure. Open-channel flows with sidewalls are also characterized by mean secondary flows that are created by turbulence. These secondary flows are Prandtl's secondary flows of the second kind. Although the secondary flows are of about 2–5% of the bulk streamwise velocity in magnitude, they affect mean flows, turbulent structures, and the transport of passive scalars such as solute contaminants, heat, and suspended sediment [1]. Since secondary flows in open-channel flows are important in engineering practices, laboratory studies or numerical simulations have been performed [2–7].

A primary tool for simulating open-channel flows involves a numerical analysis of the Reynolds-averaged Navier–Stokes (RANS) equations. Since the RANS equations do not form a closed set, a numerical solution of RANS equations requires the introduction of approximations, namely turbulence models such as the two equation model, the algebraic stress model, and the Reynolds stress model. In addition, a solution in which the RANS model is used cannot provide detailed information on the flow structure on a small scale. Recent advances in computer technologies have led to amazing developments in the area of computational fluid dynamics. Accordingly, in order to overcome the problems of the RANS approach, the Navier–Stokes equations without turbulence closure are solved directly. This is referred to as a direct numerical simulation (DNS). Since a DNS resolves all motions contained in the flow, it is recognized to be the most precise simulation tool for the analysis of turbulence structures and wall effects [8]. Moreover, DNS data on instantaneous three-dimensional velocity and pressure fields provide information that complements data collected on experimental studies on turbulent flows [9]. However, the computer requirements increase so rapidly with Reynolds number (approximately as Re^3) that the applicability of this approach is limited to flows with low Reynolds numbers. Therefore, it is almost impossible, even with today's computers, to simulate flows at high Reynolds numbers such as stream flows, using DNS. Nevertheless, the mean flow and statistics of energy-containing motions exhibit only weak Reynolds-number dependences [10], and the mechanisms driving corner secondary flows at disparate Reynolds numbers are similar [11]. For this reason, many DNS studies of turbulent flows at low Reynolds numbers have recently been performed [9, 11–16].

Although, at the present time, DNS of turbulent flows in an open-channel with sidewalls are not available, a literature survey reveals that several studies by large eddy simulation (LES), a compromise between the RANS model and DNS, have been performed. Shi *et al.* [6] performed LES of turbulent flows in a straight open-channel with sidewalls, and provided mean flow and turbulence structures. Shi *et al.* [6] concluded that the simulated results were in good agreement with previously measured data. Recently, Broglia *et al.* [17] performed LES of turbulent flows at bulk Reynolds numbers (based on the bulk streamwise velocity and the flow depth) of 5571, 9844, and 17 130 in an open-channel with sidewalls. They observed both outer and inner secondary flows near the free surface. Broglia *et al.* [17] also described in detail the mean flow properties and turbulence structures near the juncture of the free surface and the sidewall.

In the present study, a DNS of turbulent flows with low Reynolds numbers in an open-channel with sidewalls were performed. The flow at a bulk Reynolds number of 4160 in a channel with a width to depth ratio of unity is simulated. Using DNS data, the turbulence statistics of mean flow and turbulence structures are provided and are compared with previously reported numerical and experimental data. The impacts of secondary flows on turbulence statistics are discussed. In order to verify the mechanism of the generation of secondary flows and the production of Reynolds shear stress, a quadrant analysis was performed.

DOI: 10.1002/fld

NUMERICAL SIMULATIONS

Numerical methods

The three-dimensional Navier–Stokes equations for unsteady incompressible flow can be presented in the following non-dimensional form:

$$\frac{\partial u_i}{\partial x_i}=0 \tag{1}$$

$$\frac{\partial u_i}{\partial t}+\frac{\partial}{\partial x_j}u_i u_j=-\frac{\partial p}{\partial x_i}+\frac{1}{Re}\frac{\partial}{\partial x_j}\frac{\partial u_i}{\partial x_j}+\frac{1}{Fr^2}S_0\delta_{1i} \quad (i,j=1,2,3) \tag{2}$$

where x_i are the Cartesian coordinates, u_i are the velocity components in the x_i-direction, p is the pressure, S_0 is the bottom slope, δ_{ij} is Kronecker's delta, Re is the Reynolds number ($=U_0H/\nu$), and Fr is the Froude number ($=U_0/\sqrt{gH}$) (here, $H=$flow depth, $U_0=$characteristic velocity, $\nu=$kinematic viscosity of fluids, and $g=$gravitational acceleration).

A fully implicit velocity decoupling procedure reported by Kim *et al.* [18] is used to solve the governing equations. This decoupling procedure is an efficient fractional step method for computing velocity components without iterations. A multi-grid method with a fast Fourier transform in a periodic streamwise direction is employed in order to accelerate the solution convergence for the Poisson equation. A detailed procedure for the computational algorithm is described below.

The second-order central finite difference scheme and the second-order Crank–Nicholson scheme are used to discretize the governing equations in space and time, respectively, after linearizing the nonlinear convective terms by the second-order procedure [19]. The discretized governing equations at time step $n+1$ are given by

$$D\mathbf{u}^{n+1}=0+cbc \tag{3}$$

$$\frac{\mathbf{u}^{n+1}-\mathbf{u}^n}{\Delta t}+N(\mathbf{u}^{n+1})=-Gp^{n+1/2}+\left(\frac{L\mathbf{u}^{n+1}+L\mathbf{u}^n}{2Re}\right)+\mathbf{sour}+\mathbf{mbc} \tag{4}$$

where L is the discrete Laplacian operator, N is the discrete convective operator, G is the discrete gradient operator, D is the discrete divergence operator, Δt is the time increment, superscript n is the time step, and $\mathbf{sour}(=S_0\delta_{1i}/Fr^2)$ represents the source term. The boundary conditions for the velocity components are imposed on cbc and **mbc**, respectively. The matrix form of Equations (3) and (4) is factored into the block LU decomposition by Perot [20] as

$$\begin{pmatrix} A & 0 \\ D & -\Delta tDG \end{pmatrix}\begin{pmatrix} I & \Delta tG \\ 0 & I \end{pmatrix}\begin{pmatrix} \mathbf{u}^{n+1} \\ \delta p \end{pmatrix}=\begin{pmatrix} \mathbf{r} \\ 0 \end{pmatrix}+\begin{pmatrix} \mathbf{mbc} \\ cbc \end{pmatrix} \tag{5}$$

$$O(\Delta t^2)=\begin{pmatrix} \Delta tMG\delta p \\ 0 \end{pmatrix} \tag{6}$$

where $A=1/\Delta t[I+\Delta t(N-L/2Re)]$, $M=N-L/2Re$, $I=$unit matrix, $\mathbf{r}=\mathbf{u}^n/\Delta t-Gp^{n-1/2}+L\mathbf{u}^n/2Re+\mathbf{sour}$, and $\delta p=p^{n+1/2}-p^{n-1/2}$. By the approximation factorization by Dukowicz and

DOI: 10.1002/fld

Dvinsky [21] Equation (5) is expressed as

$$A\mathbf{u}^* = \mathbf{r} + \mathbf{mbc} \tag{7}$$

$$\Delta t DG\delta p = D\mathbf{u}^* - cbc \tag{8}$$

$$\mathbf{u}^{n+1} = \mathbf{u}^* - \Delta t G\delta p \tag{9}$$

$$p^{n+1/2} = p^{n-1/2} + \delta p \tag{10}$$

where $\mathbf{u}^*$ is the intermediate velocity. Equations (7)–(10) show that the velocity–pressure decoupling is attained.

As stated earlier, the approximation factorization is also extended to the velocity components ($\mathbf{u}^*$) in Equation (7) by employing $\delta\mathbf{u}^*(=\mathbf{u}^* - \mathbf{u}^n)$. Hence, Equation (7) is expressed as

$$A\delta\mathbf{u}^* = -A\mathbf{u}^{n+1} + \mathbf{r} + \mathbf{mbc} \equiv \mathbf{R} \tag{11}$$

which can be rewritten in the matrix form as

$$\frac{1}{\Delta t}\begin{pmatrix} I+\Delta t M_{11} & \Delta t M_{12} & \Delta t M_{13} \\ \Delta t M_{21} & I+\Delta t M_{22} & \Delta t M_{23} \\ \Delta t M_{31} & \Delta t M_{32} & I+\Delta t M_{33} \end{pmatrix}\begin{pmatrix} \delta u_1^* \\ \delta u_2^* \\ \delta u_3^* \end{pmatrix} = \begin{pmatrix} R_1 \\ R_2 \\ R_3 \end{pmatrix} \tag{12}$$

Using the approximation factorization of the matrix form in Equation (12), the intermediate velocity components (δu_1^*, δu_2^*, and δu_3^*) are decoupled, i.e.

$$\frac{1}{\Delta t}\begin{pmatrix} I+\Delta t M_{11} & 0 & 0 \\ \Delta t M_{21} & I+\Delta t M_{22} & 0 \\ \Delta t M_{31} & \Delta t M_{32} & I+\Delta t M_{33} \end{pmatrix}\begin{pmatrix} I & \Delta t M_{12} & \Delta t M_{13} \\ 0 & I & \Delta t M_{23} \\ 0 & 0 & I \end{pmatrix}\begin{pmatrix} \delta u_1^* \\ \delta u_2^* \\ \delta u_3^* \end{pmatrix} = \begin{pmatrix} R_1 \\ R_2 \\ R_3 \end{pmatrix} \tag{13}$$

where the intermediate velocities are computed separately by introducing new intermediate variables (δu^{**}) through the following steps:

$$\frac{1}{\Delta t}(I+\Delta t M_{11})\delta u_1^{**} = R_1 \tag{14}$$

$$\frac{1}{\Delta t}(I+\Delta t M_{22})\delta u_2^{**} = R_2 - M_{21}\delta u_1^{**} \tag{15}$$

$$\frac{1}{\Delta t}(I+\Delta t M_{33})\delta u_3^{**} = R_3 - M_{31}\delta u_1^{**} - M_{32}\delta u_2^{**} \tag{16}$$

$$\delta u_2^* = \delta u_2^{**} - \Delta t M_{23}\delta u_3^* \tag{17}$$

$$\delta u_1^* = \delta u_1^{**} - \Delta t M_{12}\delta u_2^* - \Delta t M_{13}\delta u_3^* \tag{18}$$

In the above equations, M_{ii} can be split into three parts, namely M_{ii}^1, M_{ii}^2, and M_{ii}^3, which contain the derivative of x_1, x_2, and x_3, respectively. Therefore, for example, Equation (14) can be rewritten as

$$\frac{1}{\Delta t}\{I+\Delta t(M_{11}^1 + M_{11}^2 + M_{11}^3)\}\delta u_1^{**} = R_1 \tag{19}$$

DOI: 10.1002/fld

Now, Equation (19) can be approximated to

$$\frac{1}{\Delta t}(I+\Delta t M_{11}^1)(I+\Delta t M_{11}^2)(I+\Delta t M_{11}^3)\delta u_1^{**}=R_1 \tag{20}$$

which is second-order accurate in time.

Boundary conditions and initial conditions

The free surface is assumed to be a shear-free interface. That is, the following rigid-lid condition is imposed on the free surface:

$$w=0 \tag{21a}$$

$$\frac{\partial u}{\partial z}=\frac{\partial v}{\partial z}=0 \tag{21b}$$

where Equation (21a) represents the zero deformation condition and Equation (21b) denotes the absence of shear stresses. This condition is reasonable when the Froude number is small or the wave effect is weak. At the bottom and at the sidewalls, the following no-slip condition is imposed:

$$u=v=w=0 \tag{22}$$

Periodic conditions are prescribed at both downstream and upstream boundaries. The initial conditions for the simulated flow are obtained from the velocity and pressure fields in the preceding simulation.

Applications

The Navier–Stokes equations are solved numerically in a channel of $2\pi H \times H \times H$ in the streamwise, transverse, and surface-normal directions, respectively (see Figure 1). The present domain size for the streamwise direction is sufficient to maintain the longest turbulent structure, as has been pointed out by Broglia *et al.* [17]. The mesh properties and flow conditions are given in Table I. All grid points in the streamwise directions are uniformly distributed, while a non-uniform grid

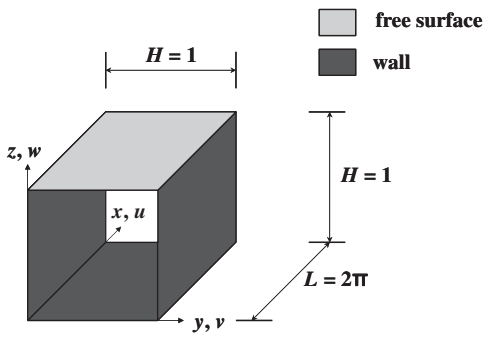

Figure 1. Schematic diagram.

DOI: 10.1002/fld

Table I. Grid properties used in the DNS.

			Grid spacing (in wall units)		
Re_B	Re_τ	# of grids (x, y, and z)	Δx^+	Δy^+ (min–max)	Δz^+ (min–max)
4160	292	64×96×96	28.67	0.91–5.10	0.91–5.10

is used in both the transverse and surface-normal directions. The following algebraic stretching is used in the transverse and surface-normal directions [22]:

$$y_j = \frac{1}{2}(b-1)\left(\frac{a^{2j/N}-1}{a^{2j/N-1}+1}\right), \quad j=0,1,\ldots,N \tag{23}$$

where $a=(b+1)/(b-1)$, $b=1.1$, and N is the number of grids in the wall-normal direction. In the computation, the maximum increment of time is $\Delta t_{\max}=0.001H/u_\tau$, and the Courant–Friedrichs–Lewy (CFL) number is fixed at unity. Mean and the second-order statistics are obtained by averaging the flow fields in time until a statistically steady state is reached.

DNS RESULTS AND DISCUSSIONS

Mean flow properties and turbulence structures

Figure 2 shows the time-averaged velocity field. In the figure, the contour map of the mean streamwise velocity (U) is presented together with the velocity vectors (V, W) for the secondary flows. All velocity components are normalized by the bulk streamwise velocity (U_B). In the contour map, the location of the maximum streamwise velocity occurs, not at the free surface, but below the free surface ($z/H \approx 0.8$). This is the so-called velocity-dip phenomenon, which is unique to turbulent open-channel flows [23].

In the half plane of the figure, two pairs of counter-rotating vortices can be seen at both the upper and lower parts of the channel section. Near the lower corner, a pair of counter-rotating secondary flows is observed, which are nearly symmetric along the corner bisector. These bottom secondary flows are similar to those observed in turbulent square duct flows by Gavrilakis [11], Huser and Biringen [14], and Joung *et al.* [24]. Near the upper corner, another pair of counter-rotating vortices is observed. However, the upper secondary flows are no longer symmetric because of the free surface. It can be seen that the maximum magnitude of the secondary flow vectors is about 3% of the bulk streamwise velocity and the point of maximum secondary flow vector is located at $y/H \approx 0.26$ and $z/H \approx 1.0$. This conforms to previous findings reported by Nezu and Rodi [2], Tominaga *et al.* [3], Naot and Rodi [4], Cokljat and Younis [5], Shi *et al.* [6] and Shiono and Feng [7]. Note also the small vortex near the upper corner. Grega *et al.* [25] first defined this small vortex as inner secondary flows to distinguish them from the outer secondary flows, the larger vortex. The size of the inner secondary flows and their magnitude are seen to be smaller than those of the outer secondary flows.

The streamlines of the secondary flows are plotted in Figure 3. These data show that the range of the inner secondary flows is narrower than the range of the outer secondary flows. According to Grega *et al.* [25], the size of the inner secondary flows is about 100 in wall units, i.e.

DOI: 10.1002/fld

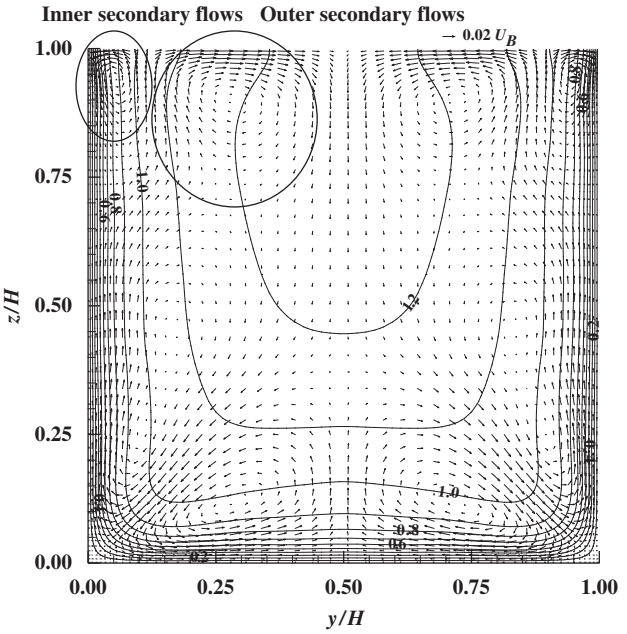

Figure 2. Time-averaged velocity field.

$y^+ = u_\tau y/\nu \approx 100$. This means that the size of the inner secondary flows is inversely proportional to the shear velocity or Reynolds number. In the present DNS, the division of inner and outer secondary flows at the free surface is about 40 in wall units. In the LES data reported by Broglia *et al.* [17], the locations of the division from their three simulation results are about $y^+ \approx 40$, which is the same as the present result.

In Figure 4, the mean streamwise velocity along the middle plane by the present DNS is compared with LES data by Broglia *et al.* [17] and measured data by Nezu and Rodi [26]. The log-law equations by Nezu and Rodi [26] from the best fit of their measured data are also plotted in the figure. Compared with the log-law, however, it can be seen that both profiles by the present DNS and by LES data by Broglia *et al.* [17] overshoot the mean streamwise velocity in the logarithmic layer below the free surface. Huser and Biringen [14] attributed this to strong turbulence production in that region. In the profiles by the present DNS and the LES data by Broglia *et al.* [17], a drop in the mean streamwise velocity near the free surface is also observed. On the whole, the origin of the discrepancy between the simulated results and the experimental data is the difference in the width-to-depth ratio. The width-to-depth ratio of the channel in the present DNS and the LES by Broglia *et al.* [17] is unity, whereas the ratio in the experiments of Nezu and Rodi [26] is 6.

Figure 5 shows the distribution of shear velocity normalized by its average value along the perimeter. In the figure, the computed results are compared with data reported by Nezu and Rodi [2]. The bulk Reynolds number of the flow in Nezu and Rodi [2] is 48 500, and the width-to-depth ratio of their channel is 2. It can be seen that the measured shear velocity increases more rapidly with distance from the corner than that in the present DNS. This conforms to Huser and Biringen [14] in that the increasing rate of the shear velocity near the wall is greater for flows with a higher Reynolds number. After a rapid increase, the shear velocity is observed to be relatively uniform.

DOI: 10.1002/fld

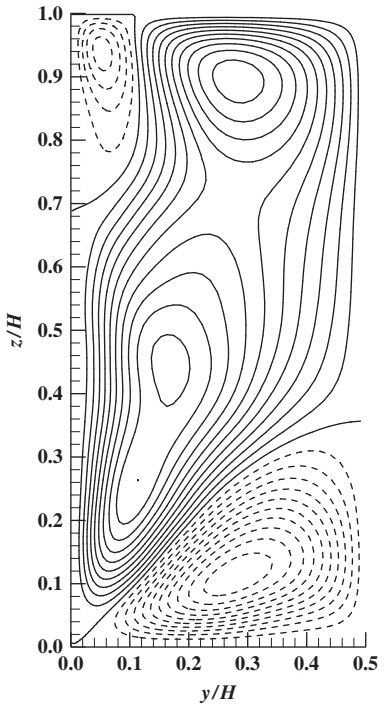

Figure 3. Streamlines for secondary flows.

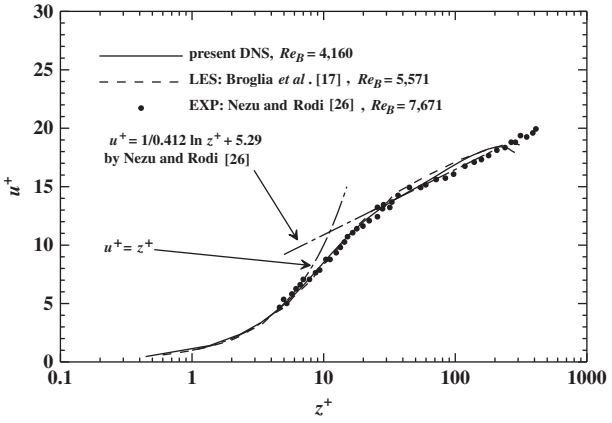

Figure 4. Streamwise mean velocity along the wall bisector in wall units.

The vertical distribution of the shear velocity along the sidewall is given in Figure 6, where the DNS results are compared with the LES data of Broglia *et al.* [17] and the measured data of Nezu and Rodi [2]. Both profiles by DNS and LES are seen to be quite similar over the depth but

DOI: 10.1002/fld

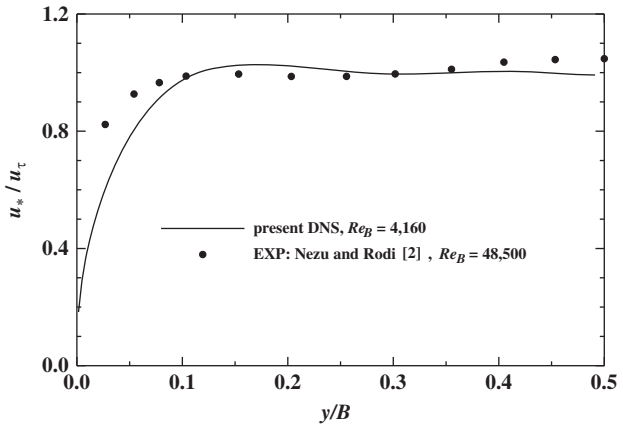

Figure 5. Shear velocity along the bottom.

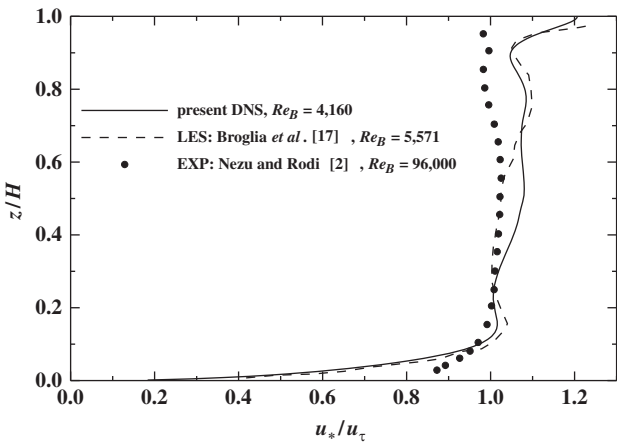

Figure 6. Shear velocity along the sidewall.

an increase in shear velocity near the free surface is not seen in the measured data. According to Broglia *et al.* [17], the inner secondary flows transfer high-momentum fluids from the free surface toward the upper corner. This is directly reflected by the shear velocity, i.e. the peak value occurs at the free surface. However, this is not observed in the data reported by Nezu and Rodi [2]. This is because the shear velocity was estimated by fitting the measured mean velocity data to the log-law for a canonical turbulent flow. In the region where the secondary flows significantly affect flow, the mean velocity profile can be considerably different from the standard logarithmic law [17]. This explains why the shear velocity determined from measured data does not show a peak near the free surface.

The contour map of the mean streamwise vorticity ($\Omega_x = \partial V/\partial z - \partial W/\partial y$) is shown in Figure 7. In the figure, the positive and negative vorticities are denoted by solid and dashed contour lines,

DOI: 10.1002/fld

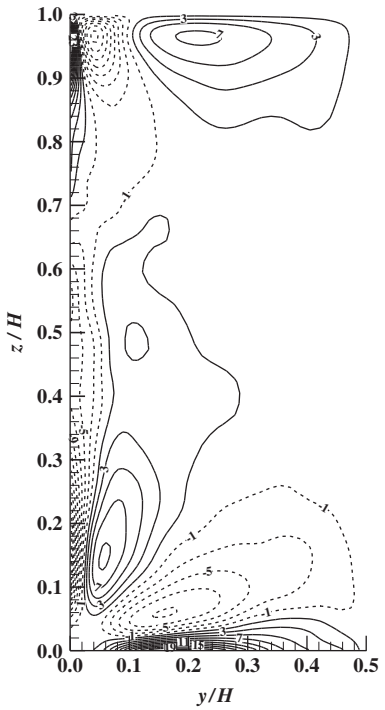

Figure 7. Distribution of mean streamwise vorticity.

respectively. Since the inner secondary flows are rotating in the counter-clockwise direction, the vorticity is negative, as can be seen in the figure. In the lower corner region, the general pattern of the vorticity is similar to that of square duct flows reported by Gavrilakis [11]. However, in the upper corner region, the free surface makes the vortical structure more complicated due to the presence of the inner and outer secondary flows.

Three components of turbulence intensity at the middle plane are shown in Figure 8. The computed results are compared with measured data by Nezu and Rodi [26] and LES data near the free surface by Broglia *et al.* [17]. It can be seen that the computed turbulence intensities near the free surface are in good agreement with the LES data of Broglia *et al.* [17]. However, turbulence intensities from the present DNS are slightly different from the profiles measured by Nezu and Rodi [26]. In the case of x-component turbulence intensity, it appears that the peak value for the measured u_{rms} is larger and the point of the measured peak is closer to the wall than the corresponding simulated data. Moser *et al.* [27], who observed the same trend, attributed this to the high Reynolds number of the flow.

Also note that the turbulence intensities show a strong anisotropy near the bottom and free surface. Near the bottom, u_{rms} appears to be dominant over the other two components. On the other hand, both u_{rms} and v_{rms} increase near the free surface and the rate of increase of v_{rms} is slightly steeper than that of u_{rms}. This is consistent with Nagaosa's [16] statement that the transfer of turbulence kinetic energy between the surface-normal and transverse direction is stronger than that between the surface-normal and the streamwise direction.

DOI: 10.1002/fld

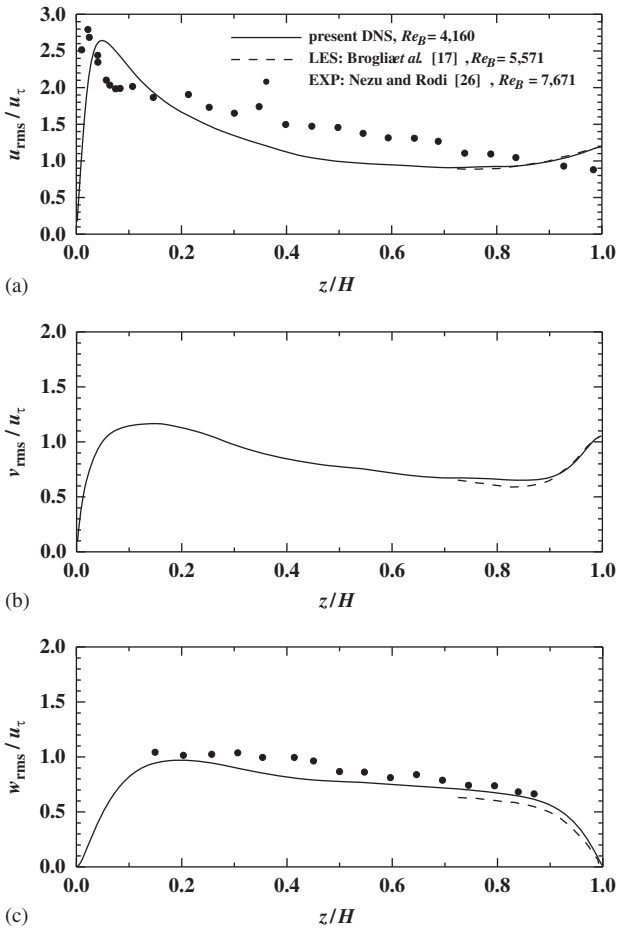

Figure 8. Turbulence intensities: (a) x-component turbulence intensity; (b) y-component turbulence intensity; and (c) z-component turbulence intensity.

Figure 9 shows contour plots of Reynolds stresses normalized by u_τ^2. In the figure, the positive and negative values are denoted by solid and dashed lines, respectively. It can be seen that the distributions of all Reynolds stress components in the region away from the free surface are similar to those for square duct flows reported by Huser and Biringen [14] and Joung *et al.* [24]. However, near the free surface, the distributions are different due to the free surface effect. Also, it turns out that the pattern of Reynolds stress components is in good agreement with LES data reported by Broglia *et al.* [17].

Figure 10 presents the surface-normal distributions for Reynolds shear stress estimated at three planes ($y/H = 0.054, 0.236$, and 0.5) using the DNS data. Joung *et al.* [24] carried out a DNS of turbulent flow in a square duct. Using the conditional quadrant analysis of the DNS data, they concluded that the patterns of the secondary flows are determined by the directional tendency of coherent structures. Huser and Biringen [14] also demonstrated the mechanism by which secondary

DOI: 10.1002/fld

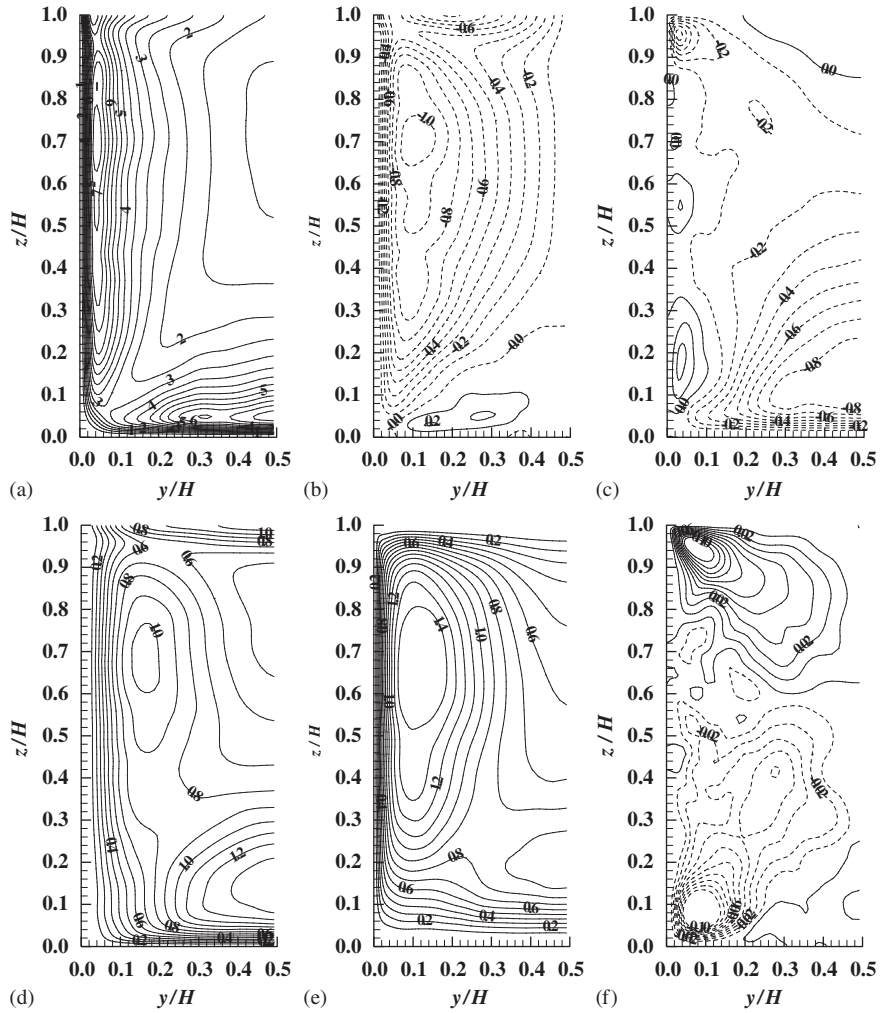

Figure 9. Contour maps of Reynolds stresses: (a) $\overline{u'^2}$; (b) $\overline{u'v'}$; (c) $\overline{u'w'}$; (d) $\overline{v'^2}$; (e) $\overline{w'^2}$; and (f) $\overline{v'w'}$.

flows are generated by connecting coherent structures to the production of Reynolds shear stresses. In the present study, the surface-normal distributions of the Reynolds shear stress are analyzed in relation to the coherent structures.

Figure 10(a) shows the surface-normal distributions for the Reynolds stress component $\overline{u'v'}$. At the middle plane, the value is zero due to symmetry. At the plane $y/H=0.236$, $\overline{u'v'}$ is positive, which is related to the bottom vortex toward the center of the channel. It then decreases continuously up to $z/H=0.7$, and abruptly increases. Thereafter, $\overline{u'v'}$ falls in the free surface region showing a minimum value. This is related to the generation of the outer secondary flows, which transfer low-momentum fluids near the wall toward the center of the channel. Overall, $\overline{u'v'}$ at $y/H=0.236$ is negative except for the region close to the bottom. At the plane close to the wall ($y/H=0.054$), $\overline{u'v'}$ has a negative value over the entire region. As a result it can be expected that

DOI: 10.1002/fld

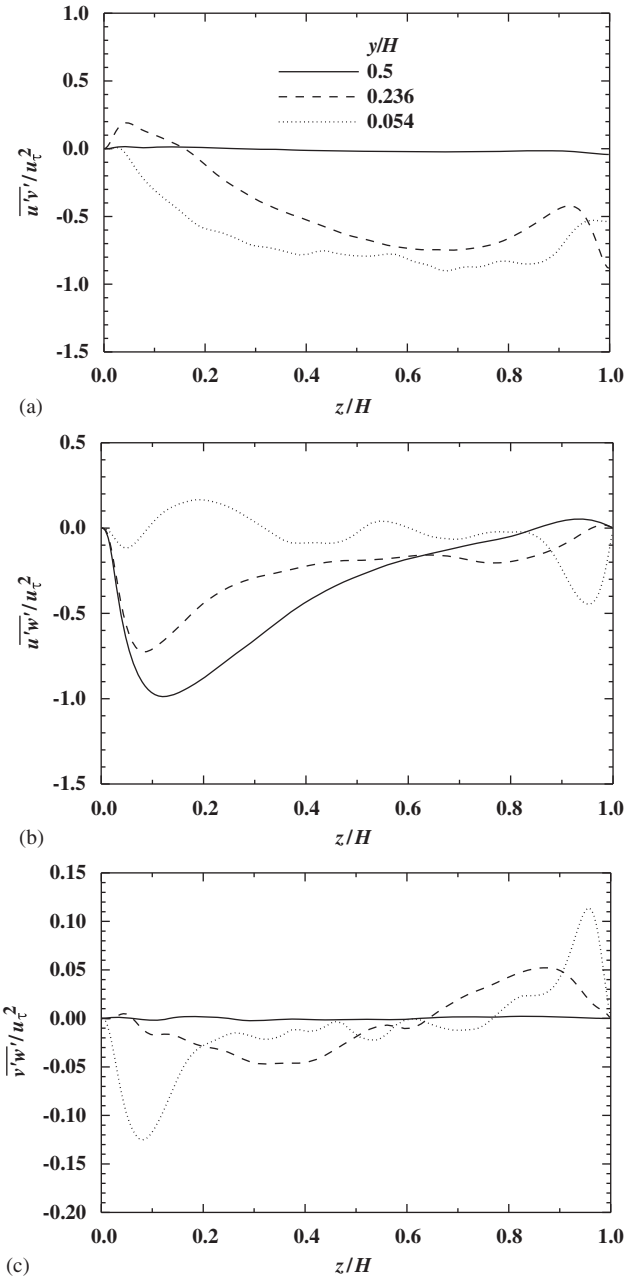

Figure 10. Surface-normal distribution of Reynolds shear stress: (a) $\overline{u'v'}$; (b) $\overline{u'w'}$; and (c) $\overline{v'w'}$.

DOI: 10.1002/fld

sweeps or ejections of coherent structures are dominant near the sidewall. $\overline{u'v'}$ at $y/H=0.054$ decreases continuously up to $z/H=0.85$. Thereafter, $\overline{u'v'}$ abruptly increases, and it then decreases slightly in the free surface region. The decrease in $\overline{u'v'}$ near the free surface is related to the inner secondary flows, which convect high-momentum fluids near the free surface toward the sidewall. The rate of decrease of $\overline{u'v'}$ at $y/H=0.054$ in the free surface region appears to be less than that at $y/H=0.236$. The difference in the rate of decrease near the free surface can be explained by the fact that the outer secondary flows are stronger than the inner secondary flows. That is, as shown in Figure 2, the region $y/H=0.054$ corresponds to the cell of the inner secondary flows, while the region $y/H=0.236$ corresponds to the cell of the outer secondary flows.

The surface-normal distributions of the Reynolds stress component $\overline{u'w'}$ are given in Figure 10(b). Both profiles at the planes $y/H=0.236$ and 0.5 show a negative Reynolds stress in the region close to the bottom. It is known that the Reynolds stress component $\overline{u'w'}$ changes linearly at the middle plane, which is not exactly true, based on the present DNS data. This seems to be the result of a sidewall effect due to the low Reynolds number of the flow. At the plane $y/H=0.054$, the Reynolds stress component is nearly positive for $z/H<0.6$. The positive Reynolds stress occurs in the region where clockwise-rotating vortices are created (see Figure 2). It would be expected that upward sweeps ($u'>0, v'<0$, and $w'>0$) and downward ejections ($u'<0$, $v'>0$, and $w'<0$) resulting in a positive $\overline{u'w'}$ at $y/H=0.054$ are dominant for this region. $\overline{u'w'}$ at $y/H=0.054$ is negative near the free surface, i.e. $z/H<0.8$, the origin of which appears to be dominant downward sweeps ($u'>0, v'<0$, and $w'<0$) and upward ejections ($u'<0$, $v'>0$, and $w'>0$) creating a negative $\overline{u'w'}$.

Figure 10(c) shows the surface-normal distributions for the Reynolds stress component $\overline{v'w'}$. It appears that the Reynolds stress component is zero due to symmetry at the middle plane. At the plane $y/H=0.236$, the Reynolds stress is negative and positive for $z/H<0.6$ and $z/H>0.6$, respectively. At the plane $y/H=0.054$, the Reynolds stress component shows the negative peak near the bottom but a positive value near the free surface. The absolute values of these peaks are observed to be larger than those at the plane $y/H=0.236$. Near the sidewall, it is likely that the negative peak near the bottom is the result of upward sweeps and downward ejections, which take place consecutively with distance from the bottom. Similarly, near the free surface, downward sweeps and upward ejections would be expected, which occur consecutively with the distance from the free surface, thus resulting in a positive peak.

In summary, sweeps and ejections of coherent structures are dominant near the sidewall (Figure 10(a)). Based on the distributions of $\overline{u'w'}$ and $\overline{v'w'}$ (Figures 10(b) and (c)), upward sweeps and downward ejections are dominant near the bottom and downward sweeps and upward ejections are dominant near the free surface. In the following, an attempt was made to relate the results obtained herein to the dominant coherent structures and secondary flow patterns using the quadrant analysis.

Instantaneous flow field

Figure 11 shows the time variations of the instantaneous streamwise velocity contour and velocity vectors (v, w) at a cross section at $x/L=0.5$. Herein, comparisons are made with the instantaneous flow fields of the turbulent square duct flow at the same passing time and space in Joung *et al.* [24]. Joung *et al*. [24] found that mushroom-shaped flow structures near all the walls of the square duct are generated or disappear with time and they are related to counter-rotating vortices. Figure 11 reveals that the instantaneous flow structures from the present DNS are different from

DOI: 10.1002/fld

those in the square duct flow near the free surface. That is, the mushroom-shaped flow structures are not generated but only dissipated near the free surface. However, near the boundaries except the free surface, the flow structures are generated and disappear, similar to the square duct flow. In addition, it appears that at the free surface, contour lines of the streamwise velocity are normal to the free surface and surface-normal velocity component is zero ($w=0$), due to the shear-free interface condition imposed in the present DNS.

Quadrant analysis

In the previous discussions, it was shown that the secondary flows are generated near the upper and lower corners of the channel and these affect the mean flows and turbulence structures. Secondary flows are found to be related to the production of Reynolds shear stresses, which is now affected by the dominant coherent structures that are generated near the wall. Herein, an attempt is made to demonstrate the generating mechanisms of secondary flows by investigating the productions of Reynolds shear stress due to dominant coherent structures. In the following discussions, at the

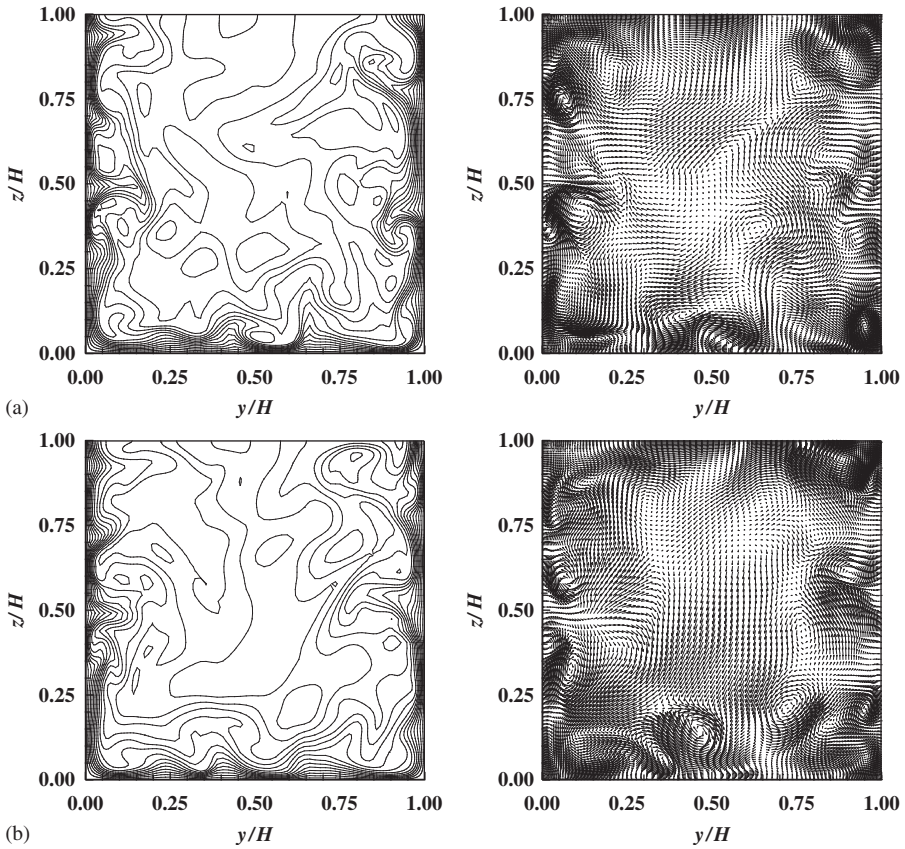

Figure 11. Time variations of instantaneous velocity fields (left: streamwise velocity u and right: velocity components (v, w)): (a) at $t=t_0$; (b) at $t=t_0+20\Delta t$; (c) at $t=t_0+40\Delta t$; and (d) at $t=t_0+60\Delta t$.

DOI: 10.1002/fld

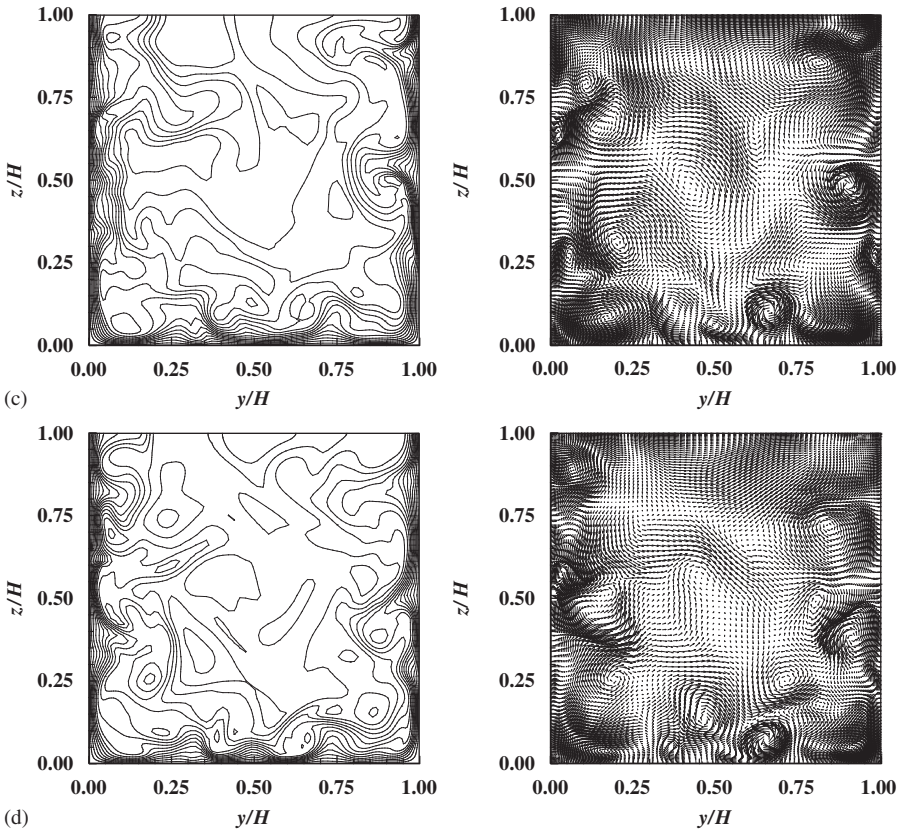

Figure 11. *Continued*.

left-hand sidewall of the channel, ejections (Q2 event) with a negative u' and positive v' denote bursting phenomena in which the low-momentum fluid at the wall is ejected into the high-speed flow. On the contrary, sweeps (Q4 event) with a positive u' and negative v' are associated with the invasion of a high-momentum fluid toward the wall.

In Figure 12, the contributions of each event to the production of primary Reynolds shear stress ($\overline{u'v'}$) near the sidewall ($y/H = 0.054$ or $y^+ \approx 14$) are presented. It can be seen in this figure that $\overline{u'v'}$ is negative for almost the entire height of the sidewall. This is because the contributions by sweeps and ejections are larger than those by Q1 and Q3 events. Near the bottom, sweeps are dominant for $z/H < 0.15$. This is related to the inrush of secondary flows toward the lower corner of the channel. It can also be seen that sweeps are dominant near the free surface, i.e. for $z/H > 0.95$. This region corresponds to the upper part of the inner secondary flows toward the sidewall. In the remaining region, the production of Reynolds stress by ejections is larger than those by sweeps, which is related to the generation of the secondary flows ejecting toward the center of the channel.

In order to investigate the relationships between the production of Reynolds shear stress ($\overline{u'v'}$) and the directional tendency of dominant coherent structures, a conditional quadrant analysis was performed. The conditional quadrant analysis is the additional consideration of the sign of

DOI: 10.1002/fld

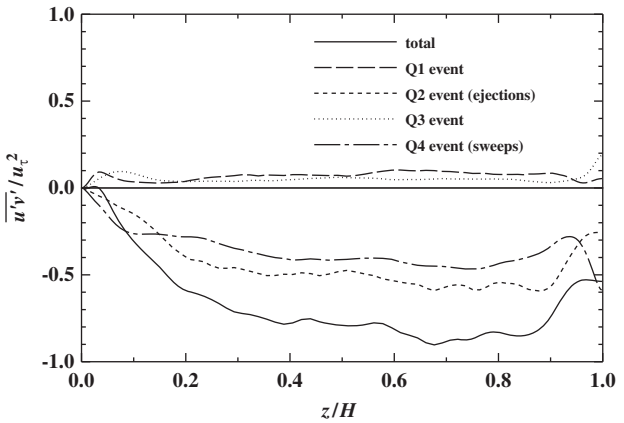

Figure 12. Production of $\overline{u'v'}$ by each event (quadrant analysis).

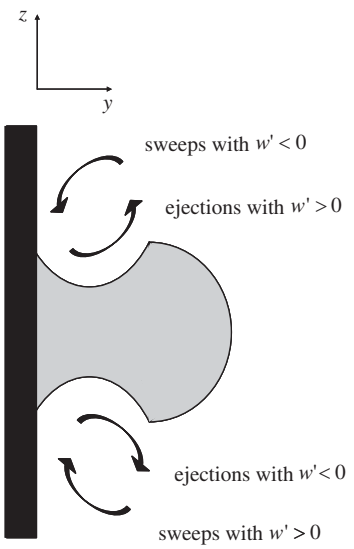

Figure 13. Definition of directional tendency of coherent structures generated near the sidewall.

w' at the points where the sweep and ejection events are dominant in the production of $\overline{u'v'}$. In Figure 13, sweeps and ejections in the conditional quadrant analysis are classified by their directional tendency in the transverse direction. Figure 14 shows the results near the sidewall ($y^+ \approx 14$). It can be seen in the figure that upward sweeps and downward ejections are dominant for $z/H < 0.15$ and for $0.15 < z/H < 0.4$, respectively. This leads to a positive $\overline{u'w'}$ and negative $\overline{v'w'}$ in the respective regions. However, production by upward ejections and downward sweeps is largest for $0.8 < z/H < 0.95$ and for $z/H > 0.95$, respectively. This results in negative $\overline{u'w'}$ and positive $\overline{v'w'}$ values in the respective regions. From the foregoing results, it appears that the production of Reynolds shear stress is determined by the directional tendency of the dominant coherent structures.

DOI: 10.1002/fld

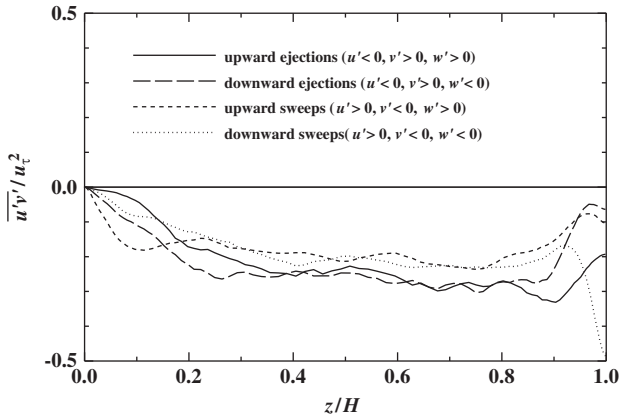

Figure 14. Production of $\overline{u'v'}$ by primary events (conditional quadrant analysis I).

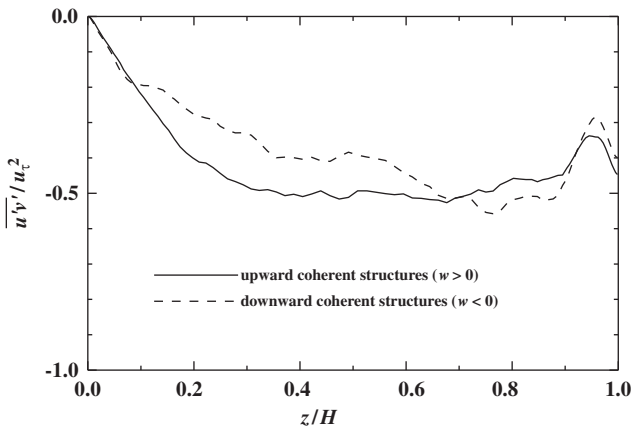

Figure 15. Production of $\overline{u'v'}$ by primary events (conditional quadrant analysis II).

However, the direction of flow in the secondary flows in Figure 2 is contrary to the results obtained by the present conditional quadrant analysis using w', i.e. ejections are heading in the opposite direction. This might be caused by the use of the fluctuating component w' instead of the instantaneous component w.

A similar conditional quadrant analysis using w was performed to see the relationship between the directional tendency of dominant coherent structures and the patterns of mean secondary flows. Figure 15 shows the production of Reynolds shear stress ($\overline{u'v'}$) by primary events near the sidewall ($y^+ \approx 14$). It can be seen in the figure that the sum of the production of Reynolds shear stress by downward sweeps and downward ejections is similar to the sum of the upward sweeps and upward ejections for $z/H < 0.08$. This implies that the generation of the secondary flows without directional tendency near the bottom. This can also be confirmed in Figure 2. For $0.08 < z/H < 0.7$, the production of $\overline{u'v'}$ by upward coherent structures is larger than that by downward coherent structures, which leads to the generation of upward secondary flows in this region. It can also

DOI: 10.1002/fld

be seen that the downward and upward coherent structures are dominant for $0.7<z/H<0.92$ and $z/H>0.92$, respectively. In these regions, the directional tendencies of dominant coherent structures correspond to the direction of the secondary flows. From the foregoing results, it can be concluded that the directional tendency of the coherent structures determines the patterns of the secondary flows.

CONCLUSIONS

This study presented a DNS of turbulent flows in an open-channel with sidewalls. The flow at a bulk Reynolds number of 4160 was simulated. The width to depth ratio of the channel is unity. The simulated data for mean flow and turbulence structures were compared with numerical and experimental data available from the literature. The DNS results were in good agreement with LES data reported by Broglia *et al.* [17] but a slight difference with the measured data was found. This is mainly due to the Reynolds number effect.

In the time-averaged velocity field, a velocity-dip phenomenon was observed, and both inner and outer secondary flows were observed, as predicted by Broglia *et al.* [17]. It appeared that the inner secondary flows significantly affect the shear velocity near the free surface although their size and magnitude are smaller than those of the outer secondary flows. It was also found that the mean streamwise velocity overshoots due to strong turbulence production in the logarithmic layer below the free surface and the turbulence intensity shows a strong anisotropy near the bottom and free surface.

Using the DNS data, relationships between Reynolds shear stress, dominant coherent structures, and the pattern of secondary flows are demonstrated. That is, it was found that the surface-normal distribution of the Reynolds shear stress components is determined by dominant coherent structures, which, in turn, create the directional tendency of the secondary flows. Through the quadrant analysis, it was shown that the production of $\overline{u'v'}$ by sweeps and ejections is larger than those by other events for the entire height near the sidewall, which results in a negative $\overline{u'v'}$ near the sidewall. Sweeps and ejections appeared to be particularly dominant near the regions where secondary flows rush in toward the sidewall and are ejected from the sidewall, respectively. Through the conditional quadrant analysis using w', it was found that the upward sweeps and downward ejections are dominant in the lower region of the channel, creating negative $\overline{u'w'}$ and positive $\overline{v'w'}$. On the other hand, in the upper region, upward ejections and downward sweeps were seen to be dominant, generating positive $\overline{u'w'}$ and negative $\overline{v'w'}$. The conditional quadrant analysis using w resulted in a directional tendency of dominant coherent structures, which precisely corresponds to the pattern of secondary flows.

NOTATION

The following symbols are used in this paper:

B	channel width
H	flow depth
L	domain size in the x-direction
p	pressure

DOI: 10.1002/fld

Re	Reynolds number ($=U_0H/\nu$)
Re_{B}	bulk Reynolds number ($=U_BH/\nu$)
Re_τ	shear Reynolds number ($=u_\tau H/\nu$)
U, V, W	mean velocity in the x-, y-, and z-directions, respectively
U_0	characteristic velocity
U_B	bulk streamwise velocity
u, v, w	instantaneous velocity components
u', v', w'	fluctuating components of velocities
u_i	velocity components in the x_i-direction
$u_{\mathrm{rms}}, v_{\mathrm{rms}}, w_{\mathrm{rms}}$	turbulence intensities
u^+	U/u_τ
u_τ	shear velocity averaged along the perimeter
u_*	local shear velocity
$\overline{u'^2}, \overline{u'v'}, \overline{u'w'}, \overline{v'^2}, \overline{v'w'}, \overline{w'^2}$	Reynolds stress components
x, y, z	streamwise, transverse, and normal to the bottom directions, respectively
y^+, z^+	distance from the wall in wall units
x_i	Cartesian coordinates
$\Delta x^+, \Delta y^+, \Delta z^+$	grid spacings in wall units
δ_{ij}	Kronecker delta
ν	kinematic viscosity and
Ω_x	mean streamwise vorticity

ACKNOWLEDGEMENTS

This research was partially supported by a grant (code No. 2-3-2) from Sustainable Water Resources Research Center of 21st Century Frontier Research Program in Ministry of Science and Technology, Korea.

REFERENCES

1. Demuren AO. Calculation of turbulence-driven secondary motion in ducts with arbitrary cross-section. *AIAA Journal* 1991; **29**(4):531–537.
2. Nezu I, Rodi W. Experimental study on secondary currents in open channel flow. *Proceeding of the 21st IAHR Congress*, Melbourne, Australia, vol. 2, 1985; 115–119.
3. Tominaga A, Nezu I, Ezaki K, Nakagawa H. Three-dimensional turbulent structure in straight open channel flows. *Journal of Hydraulic Research* (IAHR) 1989; **27**(1):149–173.
4. Naot D, Rodi W. Calculation of secondary currents in channel flow. *Journal of the Hydraulics Division* (ASCE) 1982; **108**(HY8):948–968.
5. Cokljat D, Younis BA. Second-order closure study of open-channel flows. *Journal of Hydraulic Engineering* (ASCE) 1995; **121**(2):94–107.
6. Shi J, Thomas TG, Williams JJR. Large-eddy simulation in a rectangular open channel. *Journal of Hydraulic Research* (IAHR) 1999; **37**(3):345–361.
7. Shiono K, Feng T. Turbulence measurements of dye concentration and effects of secondary flow on distribution in open channel flows. *Journal of Hydraulic Engineering* (ASCE) 2003; **129**(5):373–384.
8. Launder BE. Phenomenological modelling: present...and future? In *Whither Turbulence*? *Turbulence at the Crossroads*, Lumley JL (ed.). Lecture Notes in Physics, vol. 357. Springer: Berlin, 1990; 439–485.
9. Kim J, Moin P, Moser R. Turbulent statistics in fully developed channel flow at low Reynolds number. *Journal of Fluid Mechanics* 1987; **177**:133–166.

DOI: 10.1002/fld

10. Pope SB. *Turbulent Flows*. Cambridge University Press: Cambridge, 2000.
11. Gavrilakis S. Numerical simulation of low-Reynolds-number turbulent flow through a straight square duct. *Journal of Fluid Mechanics* 1992; **244**:101–129.
12. Lyons SL, Hanratty TJ, McLaughlin JB. Large-scale computer simulation of fully developed channel flow with heat transfer. *International Journal for Numerical Methods in Fluids* 1991; **13**:999–1028.
13. Lam K, Banerjee S. On the condition of streak formation in a bounded turbulent flow. *Physics Fluids A* 1992; **4**:306–320.
14. Huser A, Biringen S. Direct numerical simulation of turbulent flow in a square duct. *Journal of Fluid Mechanics* 1993; **257**:65–95.
15. Handler RA, Saylor JR, Leighton RI, Rovelstad AL. Transport of a passive scalar at a shear-free boundary in fully developed turbulent open channel flow. *Physics of Fluids* 1999; **11**(9):2607–2625.
16. Nagaosa R. Direct numerical simulation of vortex structures and turbulent scalar transfer across a free surface in a fully developed turbulence. *Physics of Fluids* 1999; **11**(6):1581–1595.
17. Broglia R, Pascarelli A, Piomelli U. Large-eddy simulation of ducts with a free surface. *Journal of Fluid Mechanics* 2003; **484**:223–253.
18. Kim K, Baek S-J, Sung HJ. An implicit velocity decoupling procedure for the incompressible Navier–Stokes equations. *International Journal for Numerical Methods in Fluids* 2002; **38**:125–138.
19. Beam RM, Warming RF. An implicit finite-difference algorithm for hyperbolic systems in conservation law form. *Journal of Computational Physics* 1976; **22**:87–110.
20. Perot JB. An analysis of the fractional step method. *Journal of Computational Physics* 1993; **108**:51–58.
21. Dukowicz JK, Dvinsky AS. Approximate factorization as a high order splitting for the implicit incompressible flow equations. *Journal of Computational Physics* 1992; **102**:336–347.
22. Tannehill JC, Anderson DA, Pletcher RH. *Computational Fluid Mechanics and Heat Transfer*. McGraw-Hill: New York, 1984.
23. Nezu I, Nakagawa H. *Turbulence in Open-channel Flows*. International Association for Hydraulic Research: Rotterdam, The Netherlands, 1993.
24. Joung Y, Choi S-U, Choi J-I. Direct numerical simulation of turbulent flow in a square duct: analysis of secondary flows. *Journal of Engineering Mechanics* (ASCE) 2007; **133**(2):213–221.
25. Grega LM, Wei T, Leighton RI, Neves JC. Turbulent mixed-boundary flow in a corner formed by a solid wall and a free surface. *Journal of Fluid Mechanics* 1995; **294**:17–46.
26. Nezu I, Rodi W. Open-channel flow measurements with a Laser Doppler anemometer. *Journal of Hydraulic Engineering* (ASCE) 1986; **112**(5):335–355.
27. Moser RD, Kim J, Mansour NN. Direct numerical simulation of turbulent channel flow up to $Re_\tau = 590$. *Physics of Fluids* 1999; **11**(4):943–945.

DOI: 10.1002/fld